Faraday Discussions

Cite this: DOI: 10.1039/d5fd00087d



PAPER





# Amorphization of laser-fabricated ignoble high-entropy alloy nanoparticles and its impact on surface composition and electrochemistry†

Robert Stuckert, [a] Felix Pohl, [b] Natalia Shkodich, [c] Oleg Prymak,[d] Nico Koch,[a] Ulrich Schürmann,[b] Michael Farle, [c] Lorenz Kienle,[b] Stephan Barcikowski [a] and Christoph Rehbock [a]*

Received 21st May 2025, Accepted 25th June 2025
DOI: 10.1039/d5fd00087d

High-entropy alloy nanoparticles (HEA NPs) constitute an interesting material class with high potential as heterogeneous catalysts due to their exceptional compositional and structural tunability and the complex interplay of different element-specific surface sites. Laser ablation in liquids (LAL) is a kinetically controlled synthesis method that allows the generation of colloidal HEA NPs. With Cr**Mn**FeCoNi-NPs, a facile control of the NP phase structure, switching between crystalline and amorphous *via* applied laser pulse duration, has been previously reported, attributed to the different particle solidification times and metalloidic carbon incorporation pathways. However, neither the replacement of the oxygen-affine Mn by the $sp^2$-carbon coupling element Cu, nor the transferability of the pulsed laser fabrication process from bulk target to micropowder feedstock processing, has been studied. In the present work, we use scanning transmission electron microscopy, equipped with energy-dispersive X-ray spectroscopy (STEM-EDX), high-resolution transmission electron microscopy (HRTEM), selected area electron diffraction (SAED), and X-ray diffraction (XRD) to demonstrate the transferability of internal phase structure tunability to the CrFeCoNi**Cu** alloy and confirm ns- and ps-pulsed LAL yielding amorphous and crystalline HEA NPs, respectively, with diameters of 10–40 nm. Furthermore, we examine the generation of Cr**Mn**FeCoNi and CrFeCoNi**Cu** nanoparticles by scalable, fully continuous ns-pulsed microparticle laser fragmentation in liquid (MP-LFL) using a high-power UV-laser and find the emergence of amorphous phase structures only in the Cu-containing nanoparticles, a phenomenon

[a]*Technical Chemistry I and Center for Nanointegration Duisburg-Essen (CENIDE), University of Duisburg-Essen, 45141 Essen, Germany*

[b]*Institute for Material Science, Synthesis and Real Structure, Faculty of Engineering, Christian-Albrechts University of Kiel, 24143 Kiel, Germany*

[c]*Faculty of Physics and Center for Nanointegration Duisburg-Essen (CENIDE), University of Duisburg-Essen, 47057 Duisburg, Germany*

[d]*Inorganic Chemistry and Center for Nanointegration Duisburg-Esen (CENIDE), 45141 Essen, Germany*

† Electronic supplementary information (ESI) available. See DOI: **https://doi.org/10.1039/d5fd00087d**

we attribute to copper-catalyzed carbon incorporation into the HEA NPs. These studies are complemented by a detailed characterization of the surface electrochemistry of the HEA NPs *via* alkaline cyclic voltammetry (CV) and elemental compositions in surface-near volumes, quantified by X-ray photoelectron spectroscopy (XPS). We elucidate that primarily the chemical composition (Mn *vs.* Cu) and, only to a lower extent, the phase structure (amorphous *vs.* crystalline) determine the surface potential, electrochemical stability upon multiple CV cycling, and surface element distribution of the particles. Finally, the activity of the HEA NPs in the oxygen evolution reaction (OER) is evaluated *via* linear sweep voltammetry (LSV), where we find amorphous Cr**Mn**FeCoNi HEA NPs to be more active (lower overpotential, higher current density) than their crystalline counterparts, motivating future application-focused work and transfer to other material systems and relevant reactions.

# Introduction

High-entropy alloy nanoparticles (HEA NPs), also named compositionally complex alloy (CCA) NPs or compositionally complex solid solution (CCSS) NPs[1] constitute a relatively new class of nanomaterials with high applicability in heterogeneous catalysis,[2,3] showing increased activities in nitrogen-converting reactions,[4] electrocatalytic water-splitting reactions,[5,6] and more,[3] resulting from synergistic interplay between multiple elements. HEA NPs were reported to form simple crystalline face-centered cubic (fcc),[7] body-centered cubic (bcc),[8] and hexagonal close-packed (hcp)[9] structures, while amorphous metallic glass HEA NPs have been reported as well.[10,11] However, how the phase structure (amorphous *vs.* crystalline) in HEA NPs affects electrocatalytic performance has not been addressed in detail yet, though several studies have reported an activity boost in amorphous materials compared to their crystalline counterparts, valid for different material systems and catalyzed reactions.[12–15]

Synthesis of HEA NPs has been frequently reported for noble and ignoble alloy systems, while the latter gained special interest due to lower costs and carbon footprint, and higher availability.[16] Synthesis strategies like carbothermal shock synthesis,[17] chemical reduction methods,[18] fast-moving bed pyrolysis,[19] solvothermal methods,[20] and arc-discharge[8] were reported to yield crystalline fcc, or bcc-type HEA NPs, while $FeCoNiCrMo_X$ HEA NPs formed *via* inert gas condensation,[11] CrMnFeCoNi HEA NPs *via* direct current sputtering,[10] CoFeNiLaPt HEA NPs *via* electrodeposition,[21] as well as high-entropy oxide[22] and high-entropy phosphide NPs[23] were shown to form amorphous structures. Although the aforementioned synthesis techniques give access to HEA NPs with uniformly mixed elements and an impressive number of individual elements,[17,24] they often lack flexibility, as they are restricted to the carriers they were generated on, or lack the flexibility of fabricating colloidal HEA NPs.[25] Fabrication of HEA NPs in the colloidal state allows their deposition on different support materials, providing supported catalysts with different loadings while keeping the particle size constant.[26]

Nanoparticle generation by laser synthesis and processing of colloids (LSPC)[27] yields colloidal nanoparticles without the need for additional stabilizing additives, and was shown to scale with laser power[28] to gain energy-specific mass productivities of 5–10 μg $J^{-1}$ for laser ablation in liquids (LAL)[29,30] and up to 18 μg

 

$J^{-1}$ for laser fragmentation in liquids (LFL),[31] enabling multiple grams per hour productivity.[29] The high flexibility of the used liquid[32] provides a high variety of synthesis conditions, and NP size and mass loading on the support can be freely tuned,[26] making LSPC, particularly LAL and LFL, an advantageous synthesis strategy. An emerging field in LSPC is the fragmentation of microparticles into nanoscale particles (microparticle laser fragmentation in liquid, MP-LFL) for both organic[33–35] and inorganic[31,36,37] materials down to nanocluster-sized particles (<3 nm),[31,38] which can be operated continuously.

Synthesis of colloidal HEA NPs *via* LAL has been reported in a few studies, where crystalline CrMnFeCoNi HEA NPs with uniformly mixed elements were synthesized *via* LAL in ethanol,[1,39] though minor oxide-driven segregations of Mn were reported by Tahir *et al.*, who laser-fabricated CrMnFeCoNi HEA NPs in ethanol as well.[40] Johny *et al.* compared the catalytic activity of quinary CrMnFeCoNi and senary CrMnFeCoNiMo HEA NPs *via* ns-pulsed laser ablation in acetonitrile, observing the formation of mainly amorphous HEA NPs with only minor contributions of fcc phases. The authors stated that the amorphous structure is stabilized by the formation of graphitic carbon shells that impede the crystallization of the metallic matrix.[41] As these studies utilized a bulk alloy target as starting material, it is unclear if different ablation dynamics of LAL and MP-LFL (where photomechanical effects may prominently contribute[31] due to the curved ablation surface) affect the yielded HEA nanoparticle composition and structure. Further, colloidal HEA NP generation *via* MP-LFL has not been reported before, although alloy micropowders in a well-defined composition, fabricated *via* high-energy ball milling,[42] are an attractive feedstock material for MP-LFL, promising possible scale-up optimization.

In previous experiments, we could show a structural directionality of LAL pulse duration on the internal phase structure of Cr**Mn**FeCoNi HEA NPs, yielding amorphous particles *via* ns-pulses and crystalline particles, at comparable sizes, *via* ps-pulses – a phenomenon we linked to differences in metalloidic carbon incorporation into the particles due to pulse-specific differences in particle cooling history.[43] This work addresses whether pulse-duration-driven amorphization rules may be transferable from Cr**Mn**FeCoNi to CrFeCoNi**Cu**. Furthermore, we investigate whether such amorphous HEA NPs can be obtained from a fully continuous, scalable MP-LFL process, using a ns-pulsed high-power UV laser, differentiating how process (LAL *vs.* MP-LFL) and material (**Mn** *vs.* **Cu**) specific input variables affect HEA NP formation mechanisms. This is complemented by a detailed analysis of the HEA NPs' surface chemistry and composition (using cyclic voltammetry (CV) and X-ray photoelectron spectroscopy (XPS)), a structural and compositional analysis (*via* BET, XRD, HRTEM), and by the activity of the corresponding HEA NPs in the oxygen evolution reaction (OER). The study design is summarized in Fig. 1.

## Results and discussion

### Volume-sensitive characterization of CrFeCoNiCu NPs from laser ablation in ethanol – material dependency of pulse-duration-driven amorphization rules

Firstly, we investigated how our previously proposed pulse duration-controlled amorphization mechanism in Cr**Mn**FeCoNi NPs, where ps-LAL yielded crystalline HEA NPs and ns-LAL amorphous HEA NPs,[43] is transferable to the related

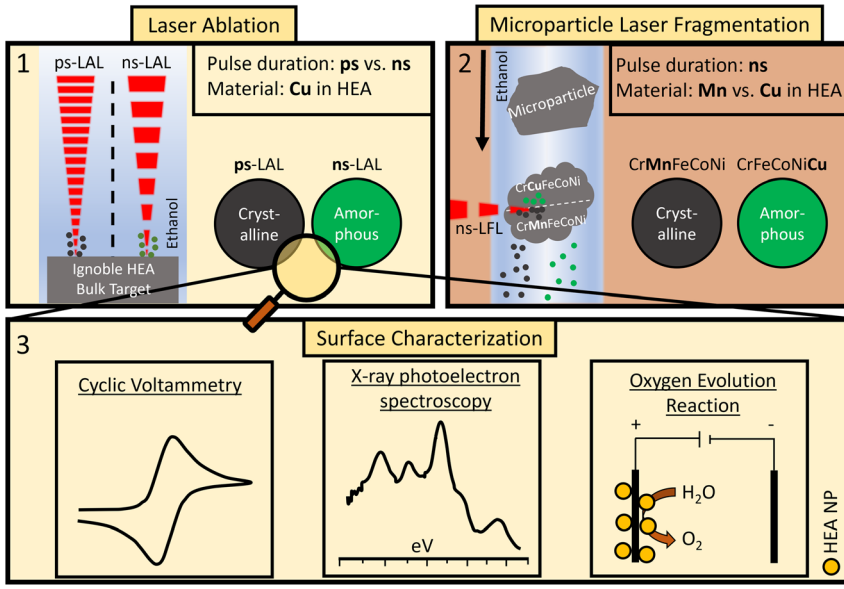


Fig. 1 Overview of the study design. (1) Investigation of pulse-duration-dependent phase control of CrFeCoNi**Cu** HEA NPs *via* laser ablation in ethanol, a phenomenon previously addressed for Cr**Mn**FeCoNi HEA NPs.[52] (2) Microparticle laser fragmentation in ethanol of Cr**Mn**FeCoNi and CrFeCoNi**Cu** microparticles with a high-power ns-pulsed UV laser, studying how the previously observed pulse-duration-dependency is transferrable to another, fully-continuous laser-based synthesis technique. (3) Electrochemical surface characterization of crystalline and amorphous Cr**Mn**FeCoNi and CrFeCoNi**Cu** HEA NPs (cyclic voltammetry and oxygen evolution reaction) in conjunction with X-ray photoelectron spectroscopy, to study compositional surface changes induced by electrochemical treatment.

CrFeCoNi**Cu** material system. LAL of CrFeCoNi**Cu** bulk targets in ethanol leads to brownish-colored colloids with mass concentrations of 100–200 mg $L^{-1}$ for both ps- and ns-LAL in ethanol, determined from differential weighing of the targets before and after ablation. The produced NPs are almost equimolar alloys, with the compositions (determined *via* large-area TEM-EDX measurements) of $Cr_{21}Fe_{22}Co_{22}Ni_{22}Cu_{13}$ for ps-LAL and $Cr_{21}Fe_{20}Co_{20}Ni_{20}Cu_{19}$ for ns-LAL (ESI, Tables S1 and S2†), which resemble the average composition of the bulk target of $Cr_{22}Fe_{22}Co_{19}Ni_{21}Cu_{17}$, as determined *via* XRF and SEM-EDX (ESI, Section S2†).

The number-weighted mean particle diameters from TEM evaluation for ps- and ns-LAL-synthesized HEA NPs are $d = 18 \pm 9$ nm and $d = 26 \pm 13$ nm, respectively (ESI, Fig. S1†). Elemental maps of individual NPs (Fig. 2a and b) show homogeneous distributions of Cr, Fe, Co, Ni, and Cu, though minor segregation can be correlated with enrichment of copper and a depletion of chromium, or *vice versa* (red arrows in Fig. 2a and b). This aligns with segregation trends in bulk,[44] microscale,[42] or nanoscale[45] HEAs, and reflects the negligible miscibility of bulk Cu and Cr,[46] though de-mixing may also be driven by Cr-oxide species. Similar segregation is observed in arc-melted CrFeCoNi**Cu** bulk targets (ESI, Fig. S2†), though overall elemental distributions in HEA NPs remain largely uniform and resemble the bulk target's surface. Interestingly, pulse-duration-driven structural

 

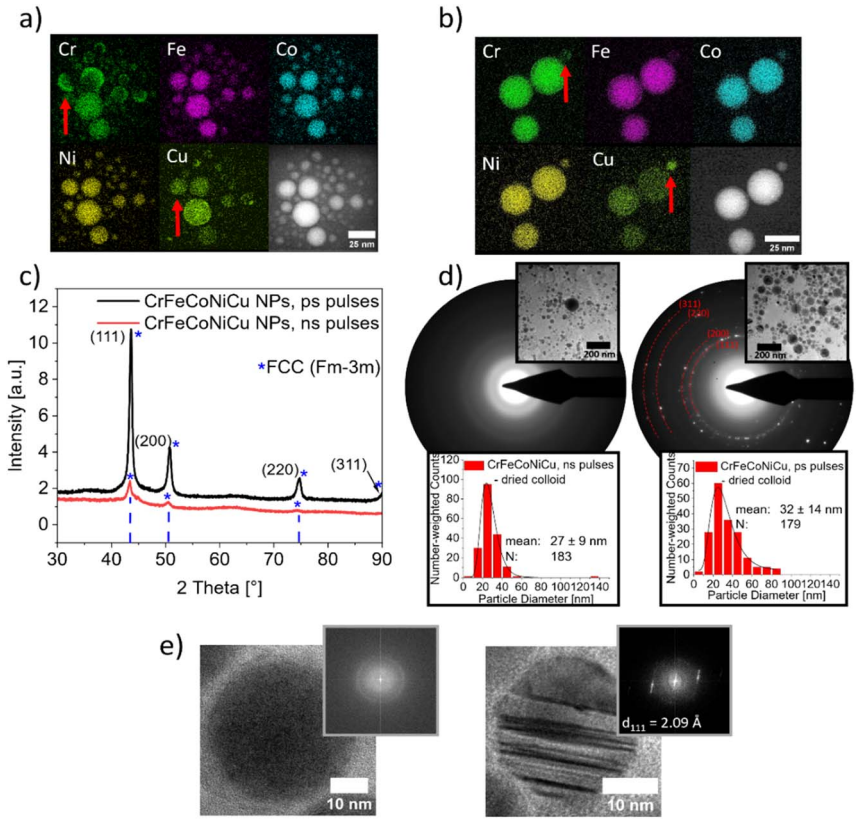


Fig. 2 STEM-EDX characterization of CrFeCoNi**Cu** HEA NPs *via* ps-LAL (a) and ns-LAL (b) with EDX maps of Cr, Fe, Co, Ni, and Cu, all data originating from K-shell signals. Additionally, structural heterogeneity of the HEA NPs is displayed in two distinct X-ray diffraction patterns of crystalline dried colloids obtained *via* ps-LAL (black) and amorphous dried colloids obtained *via* ns-LAL (red) (c), and SAED data of particle ensembles with similar mean particle diameters (shown by insets of particle size distributions) for amorphous HEA NPs obtained *via* ns-LAL (left) and crystalline HEA NPs obtained *via* ps-LAL (right) (d). HRTEM images of exemplary HEA NPs with fast Fourier transform (FFT)-insets support the observation of pulse-length-dependent structural difference in the synthesized HEA NPs, highlighting an amorphous HEA NP without reflections when obtained *via* ns-LAL and a crystalline HEA NP with a (111) reflection ($d_{111} = 0.209$ nm) when obtained *via* ps-LAL (e). The overall observations state that the postulated pulse-duration-dependent amorphization mechanism reported previously for Cr**Mn**FeCoNi[52] can be extended to the CrFeCoNi**Cu** system during laser ablation in ethanol.

heterogeneity, as reported earlier for Cr**Mn**FeCoNi HEA NPs,[1,39,41,43] occurs analogously in CrFeCoNi**Cu**, as indicated by XRD (Fig. 2c). Ps-LAL yields highly crystalline NPs with distinct reflections matching a fcc structure and two different lattice parameters ($a_1 = 0.3588$ nm, CS = 35 nm and $a_2 = 0.3602$ nm, CS = 13 nm), resembling the lattice constants found in the bulk target ($a_1 = 0.3584$ nm, $a_2 = 3.607$ nm, ESI, Section S1, Fig. S2 and Section S2, Fig. S3†), and an asymmetry in reflections, arising from the presence of the two different lattice parameters. As these two different lattice constants with equivalent values are found in the bulk

phase as well as in the NPs, we can assume that contributions of particle diameter to the lattice constant values are negligible. The presence of different lattice parameters in ps-LAL-generated CrFeCoNi**Cu** HEA NPs is likely due to Cr–Cu compositional variations, verified by single-particle EDX analysis (Tables S3 and S4, ESI†), and can be attributed to the limited mutual solubility between Cr and Cu under equilibrium conditions, despite the rapid quenching during LAL. This immiscibility can initiate nanoscale phase separation, which would lead to these different lattice parameters. In the single particle compositions, we found the standard deviations of the Cu and Cr content in individual particles to be 3–4 times and 2 times higher, respectively, than those of Fe, Co, and Ni. Similar phase distinctions have been observed before by Shkodich *et al.*, who reported lattice parameters of 0.3608 nm for Cu-rich/Cr-depleted and 0.3572 nm for Cr-rich/Cu-depleted regions in CrFeCoNi**Cu** HEA microparticles after annealing,[42] so it is conceivable that the observed differences in the lattice parameters in our observed HEA NPs also arise from Cr/Cu segregation. Moreover, note that the smaller lattice constant ($a_1 = 0.3588$ nm) is linked to larger crystallite sizes (CS = 35 nm). Even though we cannot fully exclude a potential impact of lattice strain on peak broadening, this data highlights a crystallite size that is larger than the mean particle diameter of $d = 18 \pm 9$ nm, determined from TEM (ESI, Fig. S1†). As crystallites cannot be larger than the actual particle diameter, we can assume that the crystal phase with the lattice parameter $a_1$ is primarily located in larger HEA NPs, which do not represent the majority of the particles in the sample but may still have a pronounced contribution in a volume-sensitive technique like XRD. Also note that in Fig. 2c (red line), a peak at a diffraction angle of $2\theta = 45°$ and CS = 25 nm (*via* anisotropic refinement) was detected. Identification of this peak was impossible due to its low intensity, and it is unclear what led to the formation of this unknown phase. However, the signal's low intensity and its total absence in the XRD pattern of the ps-LAL-generated HEA NPs (Fig. 2c, black line) suggest that this phase is not reproducibly formed in the majority of the sample and may be attributed to an unknown contamination of the sample.

In contrast, the CrFeCoNi**Cu** NPs synthesized *via* ns-LAL show significantly weaker reflections, which suggests that mainly amorphous NPs may be present. Additionally, reflections with low intensities, resembling metallic fcc structures, can be observed. However, the small peak intensity of the crystalline fcc structure (Fig. 2c, red line) suggests that a small portion of HEA NPs form with a crystalline structure. Considering that individual particles may experience deviating cooling rates, *e.g.*, *via* the different predicted particle formation channels during ps-LAL of silver in water,[47] we assume that a small portion of HEA NPs form without the incorporation of metalloidic carbon after cooldown and thus are able to form metallic fcc structures. This is in line with our previous observations on Cr**Mn**FeCoNi HEA NPs, where minor crystalline fractions were also reported after ns-LAL.[43]

However, note that weaker reflections may also be an effect of very small coherently scattering domains, *e.g.*, in very small, monocrystalline NPs. Thus, additional SAED (Fig. 2d) and HRTEM analysis (Fig. 2e) confirms the trends observed *via* XRD. It validates the formation of predominantly amorphous samples *via* ns-LAL (Fig. 2d and e, left) and crystalline ones *via* ps-LAL (Fig. 2d and e, right), flanked by similarity in mean particle size between the samples, which rules out that the weaker reflection intensity in the XRD pattern of Fig. 2c is

 

a particle-size-dependent phenomenon. The crystalline NPs from ps-LAL, analyzed *via* SAED, have *d*-values of 0.209 nm (111), 0.182 nm (200), 0.128 nm (220), and 0.109 nm (311) for the metallic fcc structure, agreeing well with former observed *d*-spacings determined for CrFeCoNi**Cu** HEA NPs formed *via* a pyrolytic reduction reaction by Chen *et al.*,[48] while minor reflections resulting from possible oxide species can also be detected (0.223 nm and 0.291 nm, possibly from $FeCr_2O_4$ and $CrO_2$ species [ICSD 171121 and ICSD 185888]).

To sum up, we show that by utilizing laser ablation in an organic liquid, the applicability of the pulse-duration-dependent phase formation observed for Cr**Mn**FeCoNi HEA NPs can be expanded to the CrFeCoNi**Cu** HEA system. As discussed in our previous work,[43] we attribute the prevalence of the amorphous phases to incorporation of metalloidic carbon into the NPs, verified by STEM-EDX and electron energy loss spectroscopy (EELS) measurements, where we could observe the presence of carbon inside a nanoparticle's core and differentiate the observed carbon species from graphitic carbon species in the particle's carbon shell. In ns-LAL, the heating duration of the ablation plume is significantly longer than in ps-LAL, which makes it more probable that active carbon species that form during laser-based methods[32,36] will diffuse into the NP. Upon cooldown with high cooling rates reaching up to $10^{12}$–$10^{13}$ K $s^{-1}$,[30,47] crystallization is hindered as carbon is integrated into the forming NPs, and consequently, the metastable amorphous structure of the HEA NPs can be stabilized. In contrast, in ps-LAL, the heating time of the plume is shorter, and thus a diffusion of carbon species into the plume and the liquid metal droplets is less likely. After the cooling process, fewer or no carbon species are suspected to be within the solidifying NPs. Only in the absence of carbon does the thermodynamically favored crystalline fcc structure form.[43]

## Volume-sensitive characterization of CrMnFeCoNi and CrFeCoNiCu NPs from MP-LFL in ethanol – transferring amorphization rules from LAL to MP-LFL

After extending the applicability of amorphous *vs.* crystalline phase control *via* LAL, we further aimed to elaborate on how the pulse duration effect and postulated mechanism can be applied to other laser-based NP synthesis methods. In detail, we address whether ns-MP-LFL may yield amorphous HEA metallic glass NPs. For this, we conducted microparticle LFL using a high-power UV laser with ns pulses ($\tau = 20$ ns) to produce HEA NPs and chose ethanol as the liquid medium to ensure comparability between our nanoparticles generated *via* LAL and MP-LFL.

As a starting material, Cr**Mn**FeCoNi and CrFeCoNi**Cu** HEA MP powders were utilized for HEA NP fabrication (details of fabrication in Experimental section; characterization in ESI, Section S3†). The educt HEA MPs derived from high-energy ball milling (HEBM) before MP-LFL were plate-shaped with a maximum planar length of 20 μm (exemplary SEM image shown in Fig. 3a). Their crystal structure was determined (*via* XRD) to be fcc with refined values of $A = 0.3591$ nm, CS = 14 ± 2 nm for Cr**Mn**FeCoNi HEA MPs and $A = 0.3603$ nm, CS = 9.5 ± 0.6 nm for CrFeCoNi**Cu** HEA MPs (Fig. 3a). MP-LFL of these HEA MPs yielded HEA NPs with mean diameters of 10 ± 4 nm (polydispersity index (PDI) = 0.17) for Cr**Mn**FeCoNi and 8 ± 3 nm (PDI = 0.14) for CrFeCoNi**Cu**. Large-area TEM-EDX measurements determined the compositions to be $Cr_{18}Mn_{31}Fe_{23}Co_{14}Ni_{14}$ for

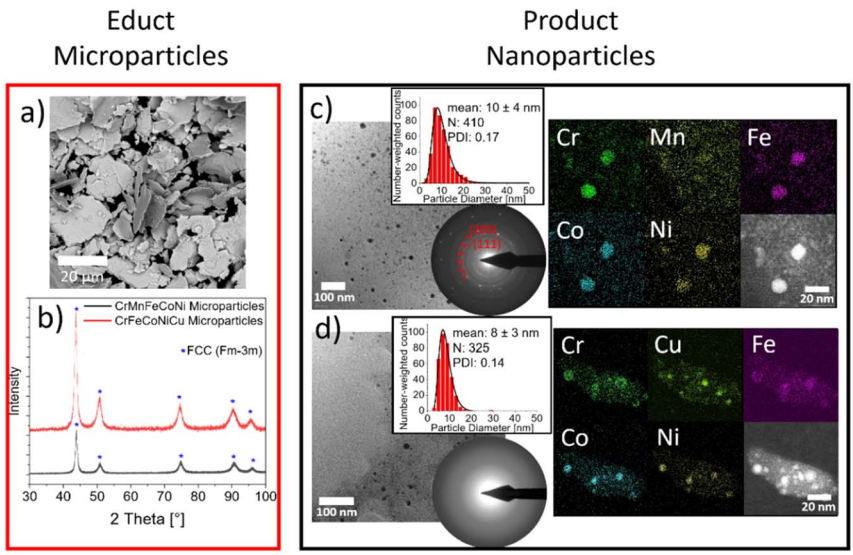


Fig. 3 MP-LFL conducted in ethanol for Cr**Mn**FeCoNi and CrFeCoNi**Cu** MPs at a fluence of 1.8 J cm$^{-2}$, synthesizing HEA NPs *via* MP-LFL. Exemplary SEM image (a) and X-ray diffraction patterns (b) of the crystalline educt Cr**Mn**FeCoNi and CrFeCoNi**Cu** MPs, showing a uniform fcc structure. TEM and SAED images with corresponding particle size distributions are complemented by exemplary STEM-EDX maps of HEA NP products generated *via* MP-LFL, for Cr**Mn**FeCoNi (c) and CrFeCoNi**Cu** (d), showing how composition sets partial segregation (Cr–Cu in Cu-containing HEA NPs) and structural development (crystalline Mn-containing HEA NPs and amorphous Cu-containing HEA NPs).

the Mn-containing alloy and $Cr_{20}Fe_{26}Co_{16}Ni_{18}Cu_{20}$ for the Cu-containing alloy (compare ESI, Tables S5 and S6†). All elements in the Cr**Mn**FeCoNi NPs were evenly distributed, except for Mn, which was less integrated into the NPs and yielded spatially more scattered signals (Fig. 3c). Considering the increased amount in the large-area EDX value, this observation could be attributed to its vapor pressure, which is the highest of all the involved elements.[49] Hence, it is conceivable that Mn, which evaporated during the synthesis process, is less integrated into the forming NPs and rather deposits as manganese oxide precipitates, as can be seen from the Mn signal in the STEM-EDX images in Fig. 3c (EDX spectra of whole area and individual HEA NP in the ESI, Section S4, Fig. S5†). This would explain the increased large-area Mn values (ESI, Table S5†) despite a less localized signal strength within the detected NPs in the EDX maps. Nonetheless, the EDX spectra show Mn peaks discernible from noise even in the diffuse areas of the map, verifying the presence of manganese (ESI, Fig. S5†). In CrFeCoNi**Cu** NPs obtained *via* MP-LFL, copper tends to segregate from the other elements, which leads to the formation of some NPs that mainly contain CrFeCoNi next to NPs dominated by copper (Fig. 3d), especially in NPs that resemble the size of the determined mean particle diameter of the samples ($d = 10 \pm 4$ nm). In contrast, in larger particles ($d$ ~25 nm), copper segregates within a particle rather than in between particles (compare ESI, Fig. S6†), agreeing with the previously observed segregations in CrFeCoNi**Cu** NPs obtained *via* LAL (Fig. 2a

and b). During MP-LFL, we observed material-dependent structural heterogeneity when analyzing the crystal structure of the product HEA NPs obtained *via* MP-LFL, as shown in the SAED analyses (Fig. 3c and d). While CrFeCoNi**Cu** HEA NPs obtained *via* MP-LFL form amorphous structures to their analogs from LAL, Cr**Mn**FeCoNi NPs from MP-LFL form crystalline structures, assigned to a metallic fcc structure ($A = 0.361$ nm; $d_{111} = 0.207$ nm, $d_{200} = 0.182$ nm). Additional reflections can be derived from crystalline oxide species. This abundance of reflections cannot be related to differences in particle size distributions, as they are comparable between samples (inset, Fig. 3c and d). Consequently, the HEA element system strongly affects the generation of amorphous HEA NPs *via* MP-LFL.

The change from LAL to MP-LFL led to the occurrence of two different phase structures (crystalline Cr**Mn**FeCoNi NPs and amorphous CrFeCoNi**Cu** NPs). In MP-LFL, the processes that dictate the size reduction of particles can be described by a photomechanical[31,34] mechanism (more dominant when ps-/fs-pulses are applied), which is favored when the pulse duration is substantially shorter than the thermal and acoustic relaxation times,[50] and when brittle materials such as oxides[31] or organic MPs[33] are used (where the inner stress from the internal pressure wave exceeds their strength). In this study, we utilize more ductile metallic MPs and laser pulses with $\tau = 20$ ns, which makes dominant photomechanical contributions to the fragmentation mechanism less likely, and the photothermal[51] effects, involving sequential heating, melting, and evaporation processes,[52] are more probable. The prevalence of photothermal processes suggests that carbon incorporation could analogously occur during the melting–evaporation process with consequent condensation of the particles. Due to the radical-forming decomposition of solvent molecules during irradiation with high-power pulsed lasers,[32,53] radical carbon species can diffuse into the inorganic precursors (atom clusters and alloy droplets) of the emerging HEA NPs to stabilize an amorphous structure upon cooling. However, the structural heterogeneity between **Cu** and **Mn**-containing HEA NPs suggests that our postulation about the carbon-diffusion-driven mechanism cannot be directly transferred from the LAL to the herein used MP-LFL process.

In LFL, cooling and solidification times are generally shorter than in LAL, though a direct comparison to literature data is limited, as the materials, educt particle sizes, and pulse durations we used differed from those in the literature.[52,54] Particle formation during NP-LFL has been predicted to set in after 200–800 ps,[52,54] whereas in LAL it is on the ns scale.[30,47] In high-fluence LFL of NPs, the fragments created by phase explosion are not trapped in the vapor bubble but are directly injected into the cold solvent, quickly cooling the created NPs.[52,54] Consequently, it can be expected that due to faster cooling, less carbon can be integrated during the formation process after LFL compared to LAL. Also, in LFL, vapor bubbles (which may contain the reactive carbon species, like radicals created from the solvent molecule) have lifetimes that are orders of magnitude shorter than during LAL.[52] This could hint towards a less efficient carbon incorporation due to a deficient availability of carbon. Moreover, emerging NPs in MP-LFL are substantially smaller than those in LAL,[31,55] making carbon incorporation even less likely, as this may also point towards faster particle growth quenching.

However, as particle formation pathways for MP-LFL of Cr**Mn**FeCoNi and CrFeCoNi**Cu** will most likely be similar, a difference in the material composition

(**Mn** *vs.* **Cu**) must be the basis for the different structural development of the HEA NPs. As carbon may be less efficiently incorporated into the NPs from MP-LFL, chemical effects like material affinity between carbon and the individual metals may be structure-determining instead. Hence, substituting **Mn** with **Cu** may lead to an altered interaction between the metal droplets/clusters and the surrounding carbon species during MP-LFL. Laser-generated Cu NPs were shown to catalyze the formation of C–C bonds and $sp^2$-carbon, resulting in C-encapsulated Cu NPs. Hence, the catalytic activity of the copper atoms may be the driving force behind this observation.[32,56,57] In contrast, after laser-based fabrication of Mn NPs in organic solvents, such structures were not observed,[58] despite the higher affinity of Mn towards C in the bulk and its molten state.[59] Thus, it is probable that the mentioned differences in the composition between the two HEA systems and the role of **Mn** or **Cu** in ruling the formation and incorporation of reactive carbon species (formed *in situ* from the organic solvent molecule) set the amorphization of HEA NPs *via* MP-LFL. In a simplified picture, we see two determinants for the final NP structure created by MP-LFL: (i) MP-LFL seems to set conditions with fast particle solidification kinetics, leading to less intensive reactions of the forming HEA NPs with their surrounding organic liquid and the reactive species created therefrom. This results in weaker amorphization tendencies during MP-LFL compared to LAL of the Cantor HEA.[43] (ii) Due to (i), material-dependent differences in the reactivity between NPs and the reactive carbon species, in this case, the faster incorporation of carbon due to Cu catalysis, become the dominant rate-limiting and structure-determining factor during particle formation. Consequently, carbon species are more quickly incorporated in the presence of Cu, hindering crystallization during the rapid cooling of HEA NPs.

The generation of HEA NPs by MP-LFL constitutes an important step towards the scale-up of HEA-NP productivity, especially when high-power UV lasers (*e.g.*, the 400 W Trumpf TruMicro 7420 as in this study) and fully continuous flow-through reactor setups are used. Spellauge *et al.* reported power-specific productivities of 18 mg $h^{-1} \times W^{-1}$ for $IrO_2$ using MP-LFL.[31] Since maximal productivity scales with material density,[28] we can benchmark against their results and anticipate comparable power-specific productivities, exceeding the values reported for LAL ($\sim$1 mg $h^{-1} \times W^{-1}$).[39,43] Consequently, utilizing such a high-power laser system, productivities of 7 g $h^{-1}$ or more become possible for the generation of HEA NPs *via* MP-LFL.

## Surface-sensitive characterization of CrFeCoNiCu and CrMnFeCoNi NPs from LAL in ethanol – impact of amorphization on electrochemical potentials and elemental composition in surface-near volumes

To gain insight into structural and compositional changes on the nanoparticle surfaces of Cr**Mn**FeCoNi and CrFeCoNi**Cu** HEA NPs obtained from ps- and ns-pulsed LAL, we conducted cyclic voltammetry (CV) measurements. A detailed characterization of the Cr**Mn**FeCoNi HEA NPs can be found in our previous work[43] and is further displayed in Section S5 of the ESI.† The central aim was to determine whether or to what extent differences in the NPs' core phase structure (amorphous *vs.* crystalline) and the core elemental composition (**Mn** *vs.* **Cu**) translate into changes in the surface electrochemical potentials. Furthermore, we aimed to elucidate the chemical stability of the surface when stressed by multiple

 

CV cycling. Thus, we carried out 100 cycles of CV in a potential window of 0–1.5 V *vs.* RHE and focused on the structural information at the surface in the untreated state (after synthesis), after the 10th cycle, and after the 100th cycle of electrochemical treatment. Note that the designation of distinct anodic/cathodic peaks in a multi-element system can be challenging due to synergistic effects resulting in peak shifts towards more positive and negative potentials.[60]

Fig. 4 displays the cyclic voltammograms of crystalline and amorphous HEA NPs of Cr**Mn**FeCoNi (Fig. 4a and b) and CrFeCoNi**Cu** (Fig. 4c and d). In both cases, the Cr**Mn**FeCoNi HEA NPs show a distinct decrease in activity throughout cycling (Fig. 4a and b). The current density of the cathodic peak (located at 0.73 V after synthesis) decreases, while a simultaneous peak shift can be observed, especially for the crystalline Cr**Mn**FeCoNi HEA NPs (Fig. 4a, shift from 0.73 V (after synthesis) to 0.47 V (after 100th cycles)). This decrease in currents in high-potential regions with consecutive electrochemical treatments hints towards an electrochemical deactivation of the HEA NP surface. The deactivation of the Cr**Mn**FeCoNi HEA was stated very recently by Luan *et al.*,[61] where Mn-rich surfaces

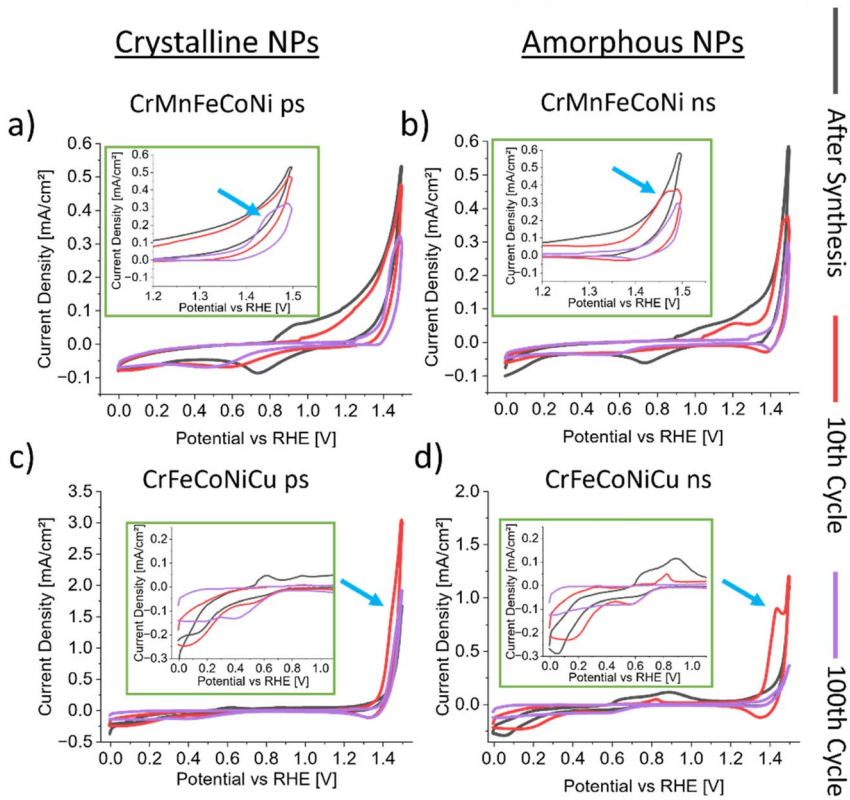


Fig. 4 Cyclic voltammograms of crystalline and amorphous HEA NPs in a potential window of 0–1.5 V *vs.* RHE in 1 M KOH with sweep rates of 20 mV $s^{-1}$. (a) Crystalline Cr**Mn**FeCoNi NPs, (b) amorphous Cr**Mn**FeCoNiCu NPs, (c) crystalline CrFeCoNi**Cu** NPs, and (d) amorphous CrFeCoNi**Cu** NPs. Insets display highlighted regions in the cyclic voltammograms to display differences in the electrochemical behavior of the HEA NPs. Blue arrows indicate the anodic current of the $NiOOH/Ni(OH)_2$ transition.

lead to deactivation and thus may also be the reason for the decrease in activity in our study. During cycling, a cathodic current appears at 1.35 V, which can be assigned to the oxidation of $Ni(OH)_2$ species to NiOOH.[62] This peak becomes more prominent in the cyclic voltammogram of the 100th cycle, where the anodic currents at 1.45 V with corresponding reduction at 1.38 V hint towards a NiOOH/$Ni(OH)_2$ transition (anodic peaks highlighted with blue arrows in Fig. 4a–d). The differences in electrochemical behavior between the surface after synthesis, after 10 cycles, and after 100 cycles of CV indicate that the structural composition of the HEA-NP surface changes with electrochemical cycling. Thus, we suspect that during CV, Ni has either moved to the nanoparticles' surface (either by diffusion or by solvation of the upper layers[61]) or was activated through an interplay with other elemental species. Interestingly, the appearance of the NiOOH/$Ni(OH)_2$ transition in amorphous Cr**Mn**FeCoNi HEA NPs (Fig. 4b) had happened already at the 10th cycle of CV, which coincides with the anodic and cathodic currents mentioned above. This suggests that the supposed movement of Ni from the core to the surface has lower activation barriers than in crystalline Cr**Mn**FeCoNi NPs. However, the 100th cycle still displays the cathodic current, whereas the anodic current cannot be observed anymore, suggesting inactivation of the previously detected Ni-species or depletion of Ni in general. This was shown to appear when inactive γ-NiOOH dominates over the more active β-NiOOH[63] species on the material's surface.[64]

In the CrFeCoNi**Cu** HEA NPs (Fig. 4c and d), new anodic and cathodic peaks appear upon substitution of Mn by Cu in the quinary alloy, particularly pronounced in the low-potential regions (0–0.9 V *vs.* RHE). These currents can thus be assigned to oxidation/reduction processes of copper species and the formation of $Cu_2O$ and $Cu(OH)_2$ on the surface of the material.[65] However, the decrease in the anodic (0.60–0.90 V *vs.* RHE) and cathodic (0–0.60 V *vs.* RHE) current densities throughout cycling depicts that the oxidation process is not fully reversible. Also, note that the broad anodic region in the previously discussed Cr**Mn**FeCoNi HEA NPs (starting at ~0.9 V *vs.* RHE) does not appear in the cyclic voltammograms of CrFeCoNi**Cu** HEA NPs, strengthening our statement about the possible Mn-species that appear in that potential region. Contrary to the Cr**Mn**FeCoNi HEA NPs in Fig. 4a and b, the CrFeCoNi**Cu** HEA NPs undergo an activation towards the 10th cycle in CV. This may be attributed to the presence of Ni-species at the NP surface. In Fig. 4c and d, distinct anodic and cathodic peaks are observable at 1.44 V *vs.* RHE (anodic peak) and 1.33 V *vs.* RHE (cathodic peak), whereas in crystalline CrFeCoNi**Cu** HEA NPs, this peak appears significantly smaller (shoulder at 1.44 V) than in amorphous CrFeCoNi**Cu** HEA NPs. Nonetheless, whether γ-NiOOH (less active in the OER) or β-NiOOH (more active in the OER) is present in that state cannot be determined based on this data.

Comparing the cyclic voltammograms of Cr**Mn**FeCoNi and CrFeCoNi**Cu** HEA NPs concerning the pulse-duration-dependent crystal structures, we can hypothesize that a distinct deactivation of the HEA nanoparticle surface is linked to the presence of Mn in the alloy, probably attributed to the formation of inactive Mn-oxide species, as shown by Luan *et al.*[61] Moreover, CrFeCoNi**Cu** HEA NPs show activation towards the 10th cycle in CV, possibly linked to the activation of Ni-species, as in both crystalline and amorphous CrFeCoNi**Cu** HEA NPs, NiOOH/$Ni(OH)_2$ transitions can be observed. Also note that the anodic and respective cathodic peaks of NiOOH/$Ni(OH)_2$ in amorphous CrFeCoNi**Cu** HEA NPs (Fig. 4d)

 

are more dominant than in the crystalline counterpart (Fig. 4c). Comparing this with the presence of the same transition species in the 10th CV cycle in amorphous Cr**Mn**FeCoNi HEA NPs (Fig. 4b) *versus* the absence in the crystalline counterpart (Fig. 4a, 10th cycle) suggests that the amorphous structure favors nickel's outward diffusion to the surface from the particles' core. The favored diffusion may be one reason that amorphous structures are favored in OER/catalysis.[66,67]

Further, we analyzed the observed surface changes (after 10 cycles and 100 cycles) in comparison to the initial (after synthesis) state *via* XPS (see details in the Experimental section) to expand our view about the already gained surface information based on electrochemical readouts. To better understand the observations on the surface electrochemistry (Fig. 4), we focus on how the surface composition (from signals emerging in the 3p region of the metallic photoelectrons) and anodic/cathodic peaks in the CV correlate (XPS spectra and tables with relative metal values are shown in the ESI, Section S6†).

Fig. 5 displays the XPS-derived changes in the surface compositions of HEA NPs before and after electrochemical treatment. For the Cr**Mn**FeCoNi HEA NPs (Fig. 5a and b), we observe a pronounced enrichment of Mn in the surface-near volume, which confirms our hypothesis of a Mn-induced electrochemical deactivation of the surface. Moreover, the statement that the outward diffusion of Ni-species from the particle cores to the surface is faster for the amorphous Cr**Mn**FeCoNi HEA NPs than for the crystalline counterpart can be strengthened by the observation of the presence of Ni at the HEA NPs' surfaces, which appears

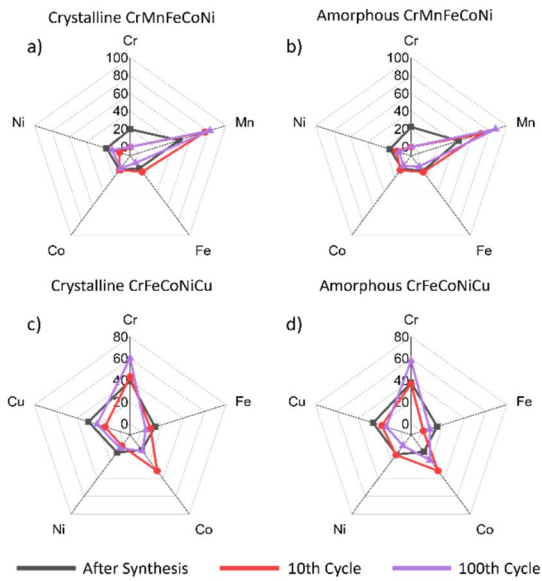


Fig. 5 Radar charts of compositional changes, derived from XPS data (see Section S6 in the ESI†), before and after cyclic voltammetry in 1 M KOH, displaying compositions [%] of the surface after synthesis, after 10 cycles of CV and after 100 cycles of CV. (a) Crystalline Cr**Mn**FeCoNi NPs, (b) amorphous Cr**Mn**FeCoNi NPs, (c) crystalline CrFeCoNi**Cu** NPs, and (d) amorphous CrFeCoNi**Cu** NPs. Note that the scales of (a)–(d) differ to support proper visibility of compositional changes.

to be higher than in the amorphous NPs in the 10th cycle (Fig. 5b), but lower in the 100th cycle, compared to the crystalline Cr**Mn**FeCoNi HEA NPs (Fig. 5a). Note that here we refer to the relative changes after the 10th and 100th cycles of CV, and that generally the Ni content is lower compared to the value before CV was conducted, most likely linked to dissolution processes upon contact with the alkaline media.[61] For CrFeCoNi**Cu**, the activation in the 10th cycle of the HEA NPs may be linked to the significantly higher proportion of Cr and Co with additional Ni at the surface (Fig. 5c and d). In contrast, in the Cr**Mn**FeCoNi HEA NPs, the relative proportion of Cr and Co is (close to) zero. Co was shown to stabilize the more active β-NiOOH species,[64] which could be the reason for higher activities in the high-potential region. However, whether Cr(–oxide) species at the surface may or may not play a role in the activation cannot be discerned based on this data. Also note that the deactivation towards the 100th cycle for CrFeCoNi**Cu** HEA NPs (Fig. 5c and d) may be linked to the oxidation of Co to $CoO_2$, which was shown to correlate with the formation of the less-active γ-NiOOH.[64] However, as the Co-proportion decreases towards the 100th cycle (Fig. 5c and d), the deactivation may also be a result of lacking Co that could otherwise stabilize β-NiOOH. Interestingly, we do not see any evidence of an electronegativity-driven activation of surface species, which is frequently discussed in the literature on Cr**Mn**FeCoNi.[5,68] Here, we do not observe any of the reported core-level shifts in our XPS spectra, where only oxidation-driven shifts could be observed (ESI, Section S6†).

In summary, we could assign anodic/cathodic currents in the cyclic voltammograms of Cr**Mn**FeCoNi/CrFeCoNi**Cu** amorphous (ns-LAL) and crystalline (ps-LAL) HEA NPs to be linked to the presence of certain species at the nanoparticle surfaces and found them to be the reason for the activation (combination of Co- and Ni-species in CrFeCoNi**Cu** HEA NPs) or deactivation (Mn-oxide species in Cr**Mn**FeCoNi HEA NPs). Furthermore, we may conclude that the morphology (crystalline *vs.* amorphous cores) has only a minute impact on the electrochemistry and surface composition, but is predominantly ruled by compositional differences when replacing Mn with Cu.

### Influence of electrochemically induced surface changes in crystalline and amorphous HEA NPs on the oxygen evolution reaction

Finally, we examined how the composition (Cu *vs.* Mn containing alloy) and the internal phase structure (crystalline *vs.* amorphous) influence the anodic electrocatalytic water splitting activity using the oxygen evolution reaction (OER) as a model electrochemical process. Finally, we correlate these findings with the surface compositions determined in the last chapter (summarized in Fig. 7). To this end, we conducted CV with consecutive linear sweep voltammetry (LSV) to understand how the NPs with different surface compositions (after synthesis, and after 10, 50, and 100 cycles of CV) perform at the OER.

Fig. 6a and c present LSV data in the 0–1.8 V *vs.* RHE range, showing current densities (CD) at 1.7 V *vs.* RHE (a) and overpotentials (OP) at 10 mA $cm_{geo}^{-2}$ (c). Initially, CrFeCoNi**Cu** HEA NPs exhibit the highest OER activity (highest CD, lowest OP), whereas Cr**Mn**FeCoNi NPs show the lowest. However, this trend reverses following electrochemical surface restructuring *via* cyclic voltammetry (CV) over 100 cycles. A direct correlation between CD loss and OP increase is observed for both systems. Among all compositions, **Mn**-containing HEA NPs demonstrate the

 

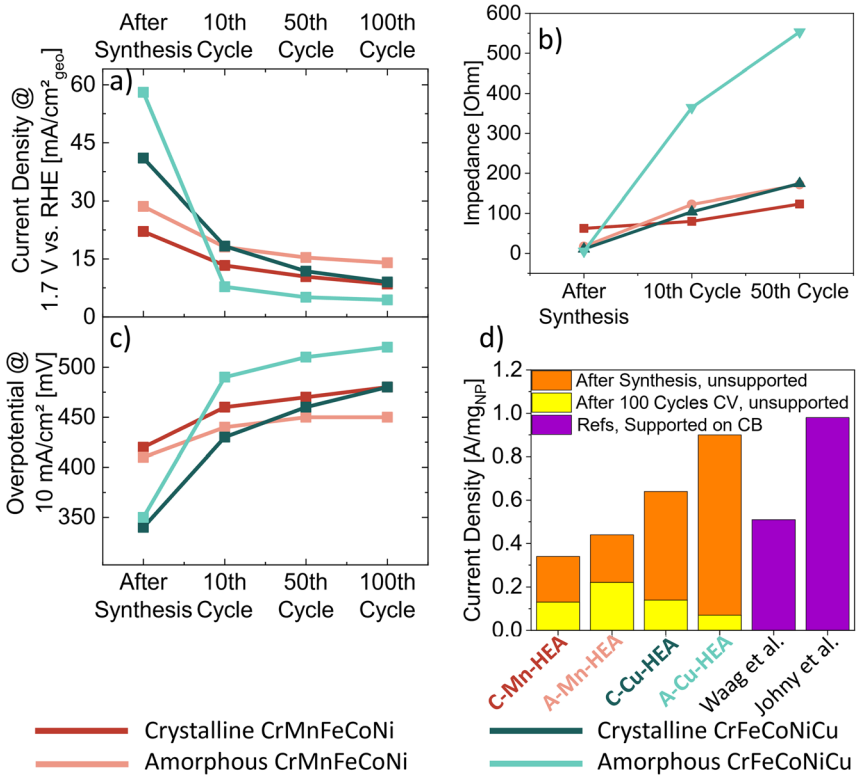


Fig. 6 OER activity of amorphous/crystalline Cr**Mn**FeCoNi and CrFeCoNi**Cu** HEA NPs, showing extracted current densities at 1.7 V *vs.* RHE (a) and overpotentials at 10 mA $cm_{geo}^{-2}$ (c) from linear sweep voltammetry experiments. (b) Impedance of HEA NPs with different states of the nanoparticle surface (after synthesis, after 10 CV cycles, and after 50 cycles) and (d) comparison of OER current densities extracted at 1.7 V *vs.* RHE: crystalline and amorphous Mn-containing HEA NPs (C-Mn-HEA and A-Mn-HEA) compared to crystalline and amorphous Cu-containing HEA NPs (C-Cu-HEA and A-Cu-HEA) as well as reference values of CB-supported HEA NPs, reported by Waag *et al.*[39] (crystalline Cr**Mn**FeCoNi HEA NPs obtained *via* ps-LAL in ethanol) and Johny *et al.*[41] (amorphous Cr**Mn**FeCoNi HEA NPs obtained *via* ns-LAL in acetonitrile).

highest stability, with CD reductions of 51% (amorphous) and 61% (crystalline) at 1.7 V *vs.* RHE. In contrast, **Cu**-containing HEA NPs, despite exhibiting superior initial performance, display the most pronounced activity losses with 78% and 92% for crystalline and amorphous nanoparticles, respectively.

Notably, CrFeCoNi**Cu** NPs show peak CD at the 10th CV cycle (Fig. 4c and d), whereas the LSV measurements reveal a continuous decline in activity from the as-synthesized state to post-CV treatment. This observation suggests that the redox-active surface intermediates discussed in the last chapter do not significantly contribute to OER catalysis under steady-state conditions. Prior studies on Cr**Mn**FeCoNi bulk electrodes by Luan *et al.*[61] proposed a transient NiFe-(oxy) hydroxide phase on top of Cr oxides as the active species, ultimately suppressed by Mn enrichment and catalyst deactivation. In our NP-based system, analogous behavior was not observed. Instead, Mn surface enrichment was shown to

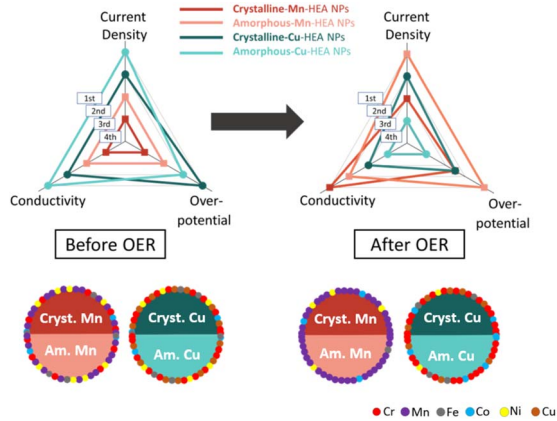


Fig. 7 Links between OER activity and surface composition. (Top row) Qualitative comparison of current density, overpotential and conductivity of crystalline and amorphous Mn- and Cu-containing HEA NPs, displaying states before (left) and after (right) the OER. The ranking of overpotential refers to the lowest overpotential being the highest-ranked material due to the highest activity. (Bottom row) Semi-quantitative evaluation of the surface composition of crystalline (cryst.) and amorphous (am.) Mn- and Cu-containing HEA NPs, displaying states before (left) and after (right) the OER. Note that each surface-localized sphere, color-coded by atom type, represents 4–5% of the total surface composition according to Table S5 (ESI).†

correlate directly with an activity decrease (Fig. 5a and b and 7). It is conceivable that the active species postulated could not be stabilized on a nanoscopic scale or that dissolution processes were faster in NPs due to a higher specific surface area, making potential active intermediate species non-observable.

In the case of CrFeCoNi**Cu** NPs, a more substantial activity decline is attributed to the enrichment of catalytically less-active Cr oxides in the surface-near region, which was reported to passivate the surface and impede outward diffusion of more active species,[61] as supported by XPS data (Fig. 5c and d). Finally, the superior performance of amorphous over crystalline Cr**Mn**FeCoNi NPs (Fig. 6a and c) is consistent with previous reports,[12–15,67,69] linking enhanced catalytic activity in amorphous materials to structural disorder and a higher density of coordinatively unsaturated sites, despite comparable surface compositions (Fig. 5a and b and 7).

Additionally, we conducted electrochemical impedance spectroscopy (EIS, raw data displayed in ESI, Section S8†) to observe possible changes in the resistance of the investigated HEA NPs (Fig. 6b), in conjunction with vacuum volumetry (based on BET adsorption) to determine the samples' specific surface area (SSA) (ESI, Section S9†). In short, three out of four HEA NP samples exhibit a modest increase in impedance (reduction in conductivity) during CV cycling, as well as an overall comparable measured SSA among samples. In these samples, we consider the impact of impedance on OER activity to be minimal. However, a stronger increase in impedance was observed for amorphous CrFeCoNi**Cu** HEA NPs, which is also linked to a lower SSA, probably attributed to particle agglomeration. For this sample, we assume that high impedance and low SSA substantially contribute to the massive loss in OER activity (Fig. 6a–c and 7). Unfortunately, this pronounced

 

increase in resistance makes it difficult to determine to what extent the structurally altered surface of CrFeCoNi**Cu** HEA NPs influences the OER activity.

We also compare the OER performance of the here-examined HEA NPs to that of laser-generated crystalline Cr**Mn**FeCoNi HEA NPs previously studied by Waag *et al.*[39] and Johny *et al.*[41] (Fig. 6d). In the literature, Waag *et al.* reported a CD of 0.51 A $mg_{NP}^{-1}$ at 1.7 V *vs.* RHE for crystalline Cr**Mn**FeCoNi HEA NPs, while Johny *et al.* reported increased activities of 0.98 A $mg_{NP}^{-1}$ at 1.7 V *vs.* RHE for amorphous Cr**Mn**FeCoNi HEA NPs. However, note that the authors in ref. 39 and 41 conducted the experiments using carbon black (CB) as the supporting material, which is known to boost catalytic activity due to the increase of the SSA of used nanoparticles[70] and was furthermore shown to increase sensitivity in charge transfer towards the glassy carbon electrode (GCE),[71] so comparability is limited. Comparing this to the initial values in our study (crystalline Cr**Mn**FeCoNi NPs: 0.34 A $mg_{NP}^{-1}$, amorphous Cr**Mn**FeCoNi NPs: 0.44 A $mg_{NP}^{-1}$, crystalline CrFeCoNi**Cu** NPs: 0.64 A $mg_{NP}^{-1}$, amorphous CrFeCoNi**Cu** NPs: 0.90 A $mg_{NP}^{-1}$ (all values recalculated from Fig. 6a)), we can state that:

(1) We could reproduce the OER activity values that Waag *et al.*[39] reported in 2019 with minor deviations (0.51 A $mg_{NP}^{-1}$ *vs.* 0.34 A $mg_{NP}^{-1}$), which is likely attributed to the supporting CB, increasing the OER activity in ref. 39. Additionally, we expanded this work and showed the activity change after 100 cycles of CV (8.5 mA $cm_{geo}^{-2}$; 0.13 A $mg_{NP}^{-1}$).

(2) Amorphous Cr**Mn**FeCoNi HEA NPs show enhanced OER activities compared to their crystalline counterpart, with initial activities of 28.6 mA $cm_{geo}^{-2}$ (0.44 A $mg_{NP}^{-1}$) and an activity of 14.0 mA $cm^{-2}$ (0.22 A $mg_{NP}^{-1}$) after 100 cycles of electrochemical cycling. This agrees with prior investigations by Johny *et al.*,[41] though deviations occur analogously due to the supporting CB in ref. 41.

(3) Though amorphous CrFeCoNi**Cu** shows a very high activity in the initial state (58.0 mA $cm_{geo}^{-2}$; 0.90 A $mg_{NP}^{-1}$), the activity decreases rapidly to 4.4 mA $cm_{geo}^{-2}$ (0.07 A $mg_{NP}^{-1}$) (associated with an increase in impedance), leaving crystalline CrFeCoNi**Cu** HEA NPs as the superior counterpart with an initial activity of 41.0 mA $cm_{geo}^{-2}$ (0.64 A $mg_{NP}^{-1}$) and 9.0 mA $cm_{geo}^{-2}$ (0.14 A $mg_{NP}^{-1}$) after 100 cycles of CV.

# Conclusions

We studied LSPC as a green and scalable technique to fabricate ignoble HEA NPs in ethanol. Previous LAL studies on Cr**Mn**FeCoNi highlighted a pulse-duration-driven mechanism controlling the particles' internal phase structure with ns-pulses and ps-pulses yielding amorphous and crystalline HEA NPs, respectively. We attribute this phenomenon to the incorporation of metalloidic carbon from the solvent's reactive species (created *in situ* by the pulsed laser process) into the forming NPs, stabilizing a metastable amorphous structure during cooldown of the alloy NP droplets. During nanosecond-LAL, the ablation plume is heated longer compared to picosecond-pulsed LAL, so the time (i) for formation of reactive carbon species, in particular molecular carbon radicals, as well as C–C coupling, and (ii) for carbon to diffuse into the NPs is extended, favoring amorphization.[43] One aim of this study was to investigate the transferability of this concept to other HEA systems, replacing Mn with Cu in the Cantor-based HEA alloy NPs. Our work confirms the transferability of the pulse-duration controlled amorphization rules to CrFeCoNi**Cu**. Based on these

findings, we may conclude that LAL constitutes a universally applicable route towards amorphous metallic glass or crystalline ignoble HEA NPs, switchable simply *via* laser pulse duration. However, further studies need to be conducted with other HEA compositions, verifying the universality of this approach and particularly the interplay between the carbon affinity of the individual HEA constituents and their activity in catalyzing solvent reactions *in situ* and carbon shell formation kinetics.

In a complementary, more scalable approach, we produced HEA NPs *via* MP-LFL, using a high-power ns-pulsed UV laser and Cr**Mn**FeCoNi and CrFeCoNi**Cu** microparticles as the starting material. Here, we verified the suitability of MP-LFL to generate HEA NPs, which may be beneficial for future upscaling approaches, as MP-LFL yields productivities higher than LAL[31] and also works in a fully continuous mode, while LAL demands target replacements at some point. Moreover, HEA MP fabrication *via* HEBM is well-established and scalable, and thus can provide starting material for MP-LFL in high quantities and with homogeneous distribution of all elements used. Interestingly, MP-LFL yielded amorphous CrFeCoNi**Cu** HEA NPs, while their **Mn**-containing counterparts were crystalline. Thus, we conclude that the particle formation pathways in LAL and MP-LFL are fundamentally different and depend on the feedstock material. Based on previous findings from large-scale molecular dynamic simulations of the NP-LFL process, we hypothesize that particle solidification pathways during MP-LFL are faster than during LAL, in that regard similar to NP-LFL,[52,54] which impairs carbon incorporation and amorphization. Here, chemical features, *e.g.*, the catalytic activity of Cu, favoring carbon shell formation, prevail. Based on these findings, we propose that the amorphization during LSPC is driven by both the kinetics and *in situ* reaction chemistry, including solidification times (setting the timescale for the structure-determining element carbon to diffuse into the particle) and chemical activity, specifically C–C bond coupling and formation of carbon shells through decomposed radical species after laser irradiation, as has been shown for Cu.[56] A more detailed structural analysis quantifying carbon contents in different regions of the particles, *e.g.*, *via* atom probe tomography, may be a suitable follow-up approach for verifying further mechanistic processes as well as expanding the HEA compositional space of the MP-LFL study, as well as the organic solvent (with different C : H : O ratios[72] or different radical-forming tendencies[36,73]).

Electrochemical characterization *via* CV and LSV of the oxygen evolution reaction in conjunction with XPS analysis enabled a correlation of electrochemical activity with the surface composition in HEA NPs, both for the crystalline and amorphous variants (Fig. 7). Hence, a compositional as well as a structural vector could be assessed. We observed that electrochemical treatment induced compositional shifts: Cr**Mn**FeCoNi NPs developed Mn-rich surfaces (with Co and Ni), correlating with a gradual decline in activity, while CrFeCoNi**Cu** NPs exhibited surfaces enriched in Cr, Co, and Cu. Pronounced $NiOOH/Ni(OH)_2$ redox peaks emerged at the 10th CV cycle in amorphous HEA NPs, suggesting lower activation barriers for outward Ni diffusion than in crystalline counterparts, where Ni signatures appeared only at later stages. These findings indicate that particle composition, specifically Mn *versus* Cu, mainly governs the surface elemental distribution, while differences in structural phase have a secondary influence, as displayed in Fig. 7, where surface compositions and also changes

 

thereof are mostly driven by the presence of **Cu** or **Mn**, respectively. This also translates into electrochemical performances in CV with redox potentials mainly driven by composition and, to a lesser extent, by the internal phase structure. OER measurements further revealed that amorphous Cr**Mn**FeCoNi NPs demonstrated improved activity and durability over 100 CV cycles, outperforming both their crystalline analogs and CrFeCoNi**Cu** NPs. This underscores the relevance of electrochemical restructuring in assessing catalyst stability. Another aspect frequently discussed in the context of HEA NPs is the impact of deviating particle size distributions on the electrochemical measurements. Here, our study highlights that in the studied HEA NPs from LSPC, different particle diameters did not show compositional differences on a single-particle level (Tables S3 and S4†). Furthermore, deviations in the TEM-derived size distributions did not translate into significant differences in specific surface areas (Table S8†), verifying that particle size effects are negligible when comparing the electrochemical performances of the herein-studied HEA nanomaterials.

We conclude that compositional tuning, especially the substitution of **Mn** with **Cu**, has the most significant impact on electrochemical behavior, while amorphization, controlled by laser pulse duration, offers an additional degree of freedom in tailoring HEA catalysts. This dual-level design approach may enhance the performance of ignoble HEA electrocatalysts.

In a nutshell we can conclude that LSPC is a scalable method for the generation of ignoble HEA NPs with internal phase structures switchable *via* pulse duration (ns *vs.* ps in LAL) and material composition (**Mn** *vs.* **Cu** in MP-LFL) based on a mechanism ruled by the interplay of particle solidification and carbon incorporation kinetics. Finally, we could deduce a structure–functionality correlation between the elemental composition in surface-near volumes and the electrochemical potential of the HEA NPs in correlation with overall composition, and to a lesser extent, the internal phase structure of the particles, verifying their applicability in electrocatalysis.

# Experimental

### Preparation of ablation targets and microparticle powders for LAL and LFL

Ablation targets for LAL NP synthesis with nominal compositions of $Cr_{20}Mn_{20}Fe_{20}Co_{20}Ni_{20}$ and $Cr_{20}Fe_{20}Co_{20}Ni_{20}Cu_{20}$ were fabricated by weighing and heat-treating metal granules of Cr, Mn, Fe, Co, Ni, and Cu (Evochem, purity 99.95–99.99%) using an arc-melting oven (AM-200, Bühler) in an argon atmosphere for melting and sintering (at 10–14 V, 50–200 A). The inert atmosphere was used to avoid oxidation of the ignoble metals. The sintered targets were remelted three times to ensure homogeneity and uniform phase formation.

HEA microparticle (HEA MP) powders were produced by high-energy ball milling (HEBM). Elemental powders of Cr, Mn, Fe, Co, Ni and Cu (purity 99.0–99.9%, grain size 10–160 μm) were used as the educt material for HEA MPs. HEBM was performed in a water-cooled planetary ball mill (Activator-2S) using stainless-steel cylindrical containers and balls (diameter = 7 mm) with a ball to powder weight ratio of 20 : 1. The process was carried out at rotation speeds (main disk/jars) of 700 rpm/1400 rpm for 120 min under dry conditions (Ar atmosphere, 4 bars, to prevent oxidation) with an additional 15 min in isopropanol. Finally, the

powder was sieved for size separation, and the grains with a size below 20 μm were used for further processing.

### HEA nanoparticle synthesis *via* bulk laser ablation and microparticle laser fragmentation

Surfactant-free HEA nanoparticles *via* LAL were synthesized in p.a. grade ethanol (VWR, purity ≥99.8%, with additional dewatering and degassing steps) to minimize oxidation of the forming nanoparticles. Before the ablation, the bulk target was additionally polished with sandpaper to ensure it was free of surface oxides. The ablation was conducted in a self-designed stirred batch reactor with a volume of 30 mL using an Nd:YAG laser (Ekspla, Atlantic Series, 10 ps, 1064 nm, 100 kHz, 0.15 mJ, $\lambda = 1064$ nm) for ps-LAL and a nanosecond-pulsed laser (Rofin, Powerline E20, 10 ns, 1064 nm, 10 kHz, 0.50 mJ, $\lambda = 1064$ nm) for ns-LAL. The nominal incident laser fluence was 0.1 J cm$^{-2}$ for ps-LAL and 7 J cm$^{-2}$ for ns-LAL. Note that in our earlier study, we showed that laser fluence does not affect the crystal structure of the HEA NPs.[43] The laser beam was moved on the target with a galvanometric scanner (100 mm focal length) in a spiral pattern.

Laser fragmentation in liquid was conducted to synthesize HEA NPs from HEA microparticle (size ≤20 μm) suspensions in ethanol (concentration = 2 g L$^{-1}$). During synthesis, the suspension was stored in a sonication bath to avoid microparticle sedimentation and ensure an evenly distributed suspension. With a peristaltic pump (ISMATEC ISM1097B), set at 115 mL min$^{-1}$, the suspended HEA microparticles were transported to an Eppendorf pipette tip (diameter of 1 mm at exit), creating a circular-shaped fluid stream with a diameter of 1 mm. A high-power nanosecond-pulsed UV laser (Trumpf, TruMicro 7420, 20 ns, 10 kHz, $\lambda = 343$ nm) at a pulse energy of 20 mJ (maximum output 40 mJ at 400 W) combined with a focusing lens was utilized to focus the laser beam perpendicularly onto the liquid stream below the circular tip exit to set a fluence of 1.8 J cm$^{-2}$ with each unit of volume being irradiated by about 5 pulses. The synthesis step was repeated four times, exposing the irradiated microparticles to a maximum of 20 pulses. The liquid stream after LFL contained a mixture of product nanoparticles and educt microparticles, which were gravimetrically separated, and characterization was conducted on the supernatants that contain the HEA NPs.

### Bulk-sensitive material characterization methods

Target characterization was done using X-ray powder diffraction (XRD, Bruker D8 Advance) with Cu K$\alpha$ radiation ($\lambda = 1.54$ Å). The measurements covered a $2\theta$ range from 5° to 130° with a step size of 0.01° and a counting time of 1.2 s to verify the crystal structure. Additionally, scanning electron microscopy combined with X-ray energy-dispersive spectroscopy (SEM-EDX, Philips XL30 equipped with an EDAX-system) and X-ray fluorescence spectroscopy (XRF, S8 Tiger, Bruker) were employed to verify the overall compositions and elemental distributions.

The global crystal structure of the fabricated HEA NPs was analyzed *via* XRD by drop-casting and drying concentrated colloidal HEA NPs of similar masses on silicon single-crystal sample holders, minimizing scattering effects. These measurements were performed using the same diffractometer (Bruker D8 Advance) within a $2\theta$ range of 30° to 90° with a step size of 0.02° and a counting time of 8 s. Qualitative phase identification was conducted with the Bruker software Diffrac Suite EVA V7.1, employing the face-centered cubic Ni phase

 

pattern (#70-1849) from the ICDD database. Lattice parameters and average crystallite size were determined through quantitative Rietveld refinement using Bruker's TOPAS 7.0 software, following instrumental calibration with a micro-crystalline $LaB_6$ standard (SRM 660b, NIST, $a = 4.15689$ Å).

Crystal structures of HEA microparticle powders were characterized *via* X-ray diffraction (Malvern Panalytical X'Pert MPD PW3040) with Cu K$\alpha$ radiation and within a $2\theta$ range of 10 to 120°. Refinements were performed utilizing Maul software[74] to determine phases, lattice parameters, and crystallite sizes (CS). For the calculation of average crystallite sizes from diffraction peak broadening in bulk and HEA NPs (using a Bruker D8 Advance) the Scherrer equation was used, and instrumental peak broadening was taken into consideration by utilizing lanthanum hexaboride ($LaB_6$; NIST; National Institute of Standards and Technology; reference compound) as an internal standard. For HEA microparticles (Malvern Panalytical X'Pert MPD PW3040), crystallite sizes were determined using the Materials Analysis Using Diffraction (MAUD) software with the Popa model, which accounts for anisotropic broadening. This model is essential for HEBM powders due to significant strain and anisotropy. A Si standard was used to separate instrumental effects, and microstrain was excluded to isolate size-related broadening. Microstructural and compositional analyses were carried out using scanning electron microscopy (SEM) (Thermo Scientic Phenom Pharos G2 Field Emission Gun (FEG)-SEM and Zeiss LEO 1530), operated in both secondary electron (SE) and backscattered electron (BSE) modes, as well as energy-dispersive X-ray spectroscopy (EDX; Oxford Instruments XMAX, 80 $mm^2$).

Transmission electron microscopy (TEM) analysis, selected area electron diffraction (SAED, *d*-value determination errors within the $\pm 0.001$ nm range), and high-resolution TEM (HRTEM) analysis were performed using a Tecnai F30 STwin $G^2$ (300 kV acceleration voltage) equipped with a Si(Li) detector (EDAX system) and a JEOL JEM 2100 (200 kV acceleration voltage). Elemental mapping was conducted using a probe-corrected JEOL JEM-ARM200F NEOARM STEM operated at 200 kV (cold-FEG) using EDX with a dual silicon drift detector system with 100 $mm^2$ active area each. All samples for (S)TEM analysis were prepared by drop-casting the NP colloid on copper grids with a lacey carbon film (Plano GmbH) or silicon nitride films (TED Pella Inc. 35 nm, 70 × 70 μm aperture). After drop-casting, all samples were dried in the atmosphere using an infrared lamp (Philips Infrared PAP38E, 150 W) for 10 min and stored under vacuum to avoid further contamination and oxidation.

### Surface-sensitive material characterization methods

The electrochemical properties of HEA NPs were investigated by utilizing a three-electrode setup, consisting of a glassy carbon working electrode (GCE, geometric area (geo) = 0.196 $cm^2$) coated with the HEA NPs *via* drop casting, a platinum wire as the counter electrode, and an Ag/AgCl reference electrode with a potentiostat (VersaSTAT, 3F, AMETEK Scientific Instruments). For all measurements (conducted at room temperature), the working electrode was coated with 12.6 μg of HEA NPs, and 1 M KOH (pH = 14) was used as the electrolyte. Before each experimental series, the electrolyte was degassed with nitrogen for 30 min and additionally for 5 min between individual measurements. Cyclic voltammetry (CV) was performed in a potential window of 0 to 1.5 V *vs.* the reversible hydrogen electrode (RHE) with sweep rates of 20 mV $s^{-1}$ for the selected (after synthesis,

10th, 100th) cycles and with 200 mV $s^{-1}$ for the cycles in between. The oxygen evolution reaction (OER) was performed by rotating the working electrode at 1600 rpm, and sweep rates of 20 mV $s^{-1}$ were utilized, reaching a maximum potential of 1.8 V *vs.* RHE, and the activity of HEA NPs was evaluated by extracting current densities at 1.7 V *vs.* RHE and overpotentials at 10 mA $cm_{geo}^{-2}$. Electrochemical impedance spectroscopy (EIS) measurements were conducted at 1.6 V *vs.* RHE and frequencies between 0.1 Hz and 100 kHz. Impedance values were determined *via* fitting the Nyquist plot using ECLab software. The model circuit for fitting is displayed in the ESI (Figure S9).†

X-ray photoelectron spectroscopy (XPS) measurements were conducted with a VersaProbe IITM from Ulvac-Phi using the Al-K$\alpha$ line at 1486.6 eV and a spot size of 100 μm with an energy resolution of 0.5 eV. A dual-beam charge neutralization was applied and a hemispherical analyzer (at an angle of 45° between sample surface and analyzer) was used for the measurements. All high-resolution spectra were corrected according to the binding energy of graphitic carbon (284.8 eV), determined during deconvolution of the C 1s spectrum of each sample. Peak deconvolution was performed using the CasaXPS software, applying a Shirley-type background and Lorentzian asymmetric curves for fitting. Quantification of relative compositional values of all metals was done by analyzing their respective 3p spectra. A meaningful analysis of the 2p region was impossible as there is an overlap with element-specific Auger lines, a drawback previously reported when analyzing ignoble HEA bulk materials[75] and even more critical during analysis of NPs, where signal intensities are generally lower.

Vacuum volumetry based on Brunauer–Emett–Teller (BET) isotherms was performed on a NOVA 800 (Anton Paar), utilizing nitrogen physisorption for determining the specific surface area (SSA) of high-entropy alloy nanoparticles. All measurements were conducted at 200 °C and the SSA was determined using the BET model with a 7-point adsorption isotherm at relative pressures of 0.05 to 0.20$p/p_0$.

## Data availability

The data that support the findings of this study are available from the corresponding author, C. R., upon reasonable request.

## Author contributions

Robert Stuckert: investigation, methodology, visualization, formal analysis, writing – original draft. Felix Pohl: investigation, formal analysis, writing – review & editing. Natalia Shkodich: investigation, resources, formal analysis, writing – review & editing. Oleg Prymak: investigation, formal analysis. Nico Koch: investigation, writing – review & editing. Ulrich Schürmann: supervision, funding acquisition, writing – review & editing. Michael Farle: funding acquisition, writing – review & editing. Lorenz Kienle: funding acquisition, supervision, writing – review & editing. Stephan Barcikowski: funding acquisition, writing – review & editing, project administration. Christoph Rehbock: visualization, supervision, project administration, writing – original draft.

## Conflicts of interest

There are no conflicts to declare.

## Acknowledgements

The authors thank the Deutsche Forschungsgemeinschaft (DFG) for financial support within the project Nr. 277627168 and DFG large scientific instrument (Nr. 491146928). N. F. Sh. and M. F. are grateful for the financial support from the DFG within CRC/Trr270, projects A04 (Project ID 405553726), and project FA209/27-1. Support by the Interdisciplinary Center for Analytics on the Nanoscale (ICAN) of the University of Duisburg-Essen (DFG RIsources reference: RI_00313), a DFG-registered core facility (Project No. 233512597 and 324659309), is gratefully acknowledged. R. S. thanks Tobias Bessel for conducting BET measurements and Florian de Kock for bulk target sintering. R. S. acknowledges Varatharaja Nallathambi and Jan Söder for fruitful scientific discussions.

## References

1 T. Löffler, F. Waag, B. Gökce, A. Ludwig, S. Barcikowski and W. Schuhmann, *ACS Catal.*, 2021, **11**, 1014–1023.

2 (*a*) W. Al Zoubi, R. A. K. Putri, M. R. Abukhadra and Y. G. Ko, *Nano Energy*, 2023, **110**, 108362, DOI: **10.1016/j.nanoen.2023.108362**; (*b*) T. G. Ritter, S. Pappu and R. Shahbazian-Yassar, *Adv. Energy Sustainability Res.*, 2024, **5**, 2300297.

3 X. Huang, G. Yang, S. Li, H. Wang, Y. Cao, F. Peng and H. Yu, *J. Energy Chem.*, 2022, **68**, 721–751, DOI: **10.1016/j.jechem.2021.12.026**.

4 (*a*) P. Xie, Y. Yao, Z. Huang, Z. Liu, J. Zhang, T. Li, G. Wang, R. Shahbazian-yassar, L. Hu and C. Wang, *Nat. Commun.*, 2019, **10**, 4011, DOI: **10.1038/s41467-019-11848-9**; (*b*) D. Zhang, H. Zhao, X. Wu, Y. Deng, Z. Wang, Y. Han, H. Li, Y. Shi, X. Chen, S. Li, J. Lai, B. Huang and L. Wang, *Adv. Funct. Mater.*, 2021, **31**, 2006939, DOI: **10.1002/adfm.202006939**.

5 H. Zhu, S. Sun, J. Hao, Z. Zhuang, S. Zhang, T. Wang, Q. Kang, S. Lu, X. Wang, F. Lai, T. Liu, G. Gao, M. Du and D. Wang, *Energy Environ. Sci.*, 2023, **16**, 619–628, DOI: **10.1039/D2EE03185J**.

6 (*a*) Y. Yu, F. Xia, C. Wang, J. Wu, X. Fu, D. Ma, B. Lin, J. Wang, Q. Yue and Y. Kang, *Nano Res.*, 2022, **15**, 7868–7876, DOI: **10.1007/s12274-022-4432-1**; (*b*) X. Li, J. Cao, G. Chen, J. Xie, C. Gu, X. Li, F. C. Walsh, Y. Wang and W. Hu, *ACS Nano*, 2025, **19**, 7851–7863.

7 (*a*) Y. Feng, H. Yao, Z. Sun, Y. Liao, J. Wang, R. Zhao and Y. Li, *ACS Appl. Mater. Interfaces*, 2024, **16**, 41027–41035; (*b*) G. R. Dey, C. R. McCormick, S. S. Soliman, A. J. Darling and R. E. Schaak, *ACS Nano*, 2023, **17**, 5943–5955; (*c*) R. Nandan, G. Raj and K. K. Nanda, *ACS Appl. Mater. Interfaces*, 2022, **14**, 16108–16116.

8 A. Mao, P. Ding, F. Quan, T. Zhang, X. Ran, Y. Li, X. Jin and X. Gu, *J. Alloys Compd.*, 2018, **735**, 1167–1175, DOI: **10.1016/j.jallcom.2017.11.233**.

9 T.-H. Hu, C.-Y. Wu, Z. Y. He, Y. Chen, L.-C. Hsu, C.-W. Pao, J.-T. Lin, C.-W. Chang, S.-C. Lin, R. Osmundsen, L. Casalena, K. H. Lin, S. Zhou and T.-H. Yang, *Adv. Sci.*, 2025, **12**, e2409023, DOI: **10.1002/advs.202409023**.

10 A. Garzón-Manjón, H. Meyer, D. Grochla, T. Löffler, W. Schuhmann, A. Ludwig and C. Scheu, *Nanomaterials*, 2018, **8**, 903, DOI: **10.3390/nano8110903**.
11 X. Zhou, H. Zhu, S. Fu, S. Lan, H. Hahn, J. Zeng and T. Feng, *Small*, 2024, e2405596, DOI: **10.1002/smll.202405596**.
12 Y. Pei, G. Zhou, N. Luan, B. Zong, M. Qiao and F. F. Tao, *Chem. Soc. Rev.*, 2012, **41**, 8140–8162, DOI: **10.1039/C2CS35182J**.
13 G. Shi, T. Tano, D. A. Tryk, M. Yamaguchi, A. Iiyama, M. Uchida, K. Iida, C. Arata, S. Watanabe and K. Kakinuma, *ACS Catal.*, 2022, **12**, 14209–14219.
14 A. Indra, P. W. Menezes, N. R. Sahraie, A. Bergmann, C. Das, M. Tallarida, D. Schmeißer, P. Strasser and M. Driess, *J. Am. Chem. Soc.*, 2014, **136**, 17530–17536.
15 Z. Jia, Q. Wang, L. Sun, Q. Wang, L.-C. Zhang, G. Wu, J.-H. Luan, Z.-B. Jiao, A. Wang, S.-X. Liang, M. Gu and J. Lu, *Adv. Funct. Mater.*, 2019, **29**, 1807857, DOI: **10.1002/adfm.201807857**.
16 L. Han, W. Mu, S. Wei, P. K. Liaw and D. Raabe, *Sci. Adv.*, 2024, **10**, eads3926.
17 Y. Yao, Z. Huang, P. Xie, S. D. Lacey, R. J. Jacob, H. Xie, F. Chen, A. Nie, T. Pu, M. Rehwoldt, D. Yu, M. R. Zachariah, C. Wang, R. Shahbazian-yassar, J. Li and L. Hu, *Science*, 2018, **359**, 1489–1494, DOI: **10.1126/science.aan5412**.
18 N. Kar, M. McCoy, J. Wolfe, S. L. A. Bueno, I. H. Shafei and S. E. Skrabalak, *Nat. Synth.*, 2024, **3**, 175–184, DOI: **10.1038/s44160-023-00409-0**.
19 S. Gao, S. Hao, Z. Huang, Y. Yuan, S. Han, L. Lei, X. Zhang, R. Shahbazian-yassar and J. Lu, *Nat. Commun.*, 2020, **11**, 2016, DOI: **10.1038/s41467-020-15934-1**.
20 D. Wu, K. Kusada, T. Yamamoto, T. Toriyama, S. Matsumura, S. Kawaguchi, Y. Kubota and H. Kitagawa, *J. Am. Chem. Soc.*, 2020, **142**, 13833–13838.
21 M. W. Glasscott, A. D. Pendergast, S. Goines, A. R. Bishop, A. T. Hoang, C. Renault and J. E. Dick, *Nat. Commun.*, 2019, **10**, 2650, DOI: **10.1038/s41467-019-10303-z**.
22 W. Rong, Y. Chen, R. Dang, K. Huang, J. Xia, B. Zhang, J. Liu, H. Meng, Q. Cao and J. Wu, *J. Alloys Compd.*, 2024, **971**, 172786, DOI: **10.1016/j.jallcom.2023.172786**.
23 Y. Wei, X. Liu, R. Yao, J. Qian, Y. Yin, D. Li and Y. Chen, *J. Alloys Compd.*, 2023, **938**, 168610, DOI: **10.1016/j.jallcom.2022.168610**.
24 Y. Liao, Y. Li, R. Zhao, J. Zhang, L. Zhao, L. Ji, Z. Zhang, X. Liu, G. Qin and X. Zhang, *Natl. Sci. Rev.*, 2022, **9**, nwac041, DOI: **10.1093/nsr/nwac041**.
25 (*a*) M. Lau, A. Ziefuss, T. Komossa and S. Barcikowski, *Phys. Chem. Chem. Phys.*, 2015, **17**, 29311–29318, DOI: **10.1039/C5CP04296H**; (*b*) S. Kohsakowski, R. Streubel, I. Radev, V. Peinecke, S. Barcikowski, G. Marzun and S. Reichenberger, *Appl. Surf. Sci.*, 2019, **467–468**, 486–492, DOI: **10.1016/j.apsusc.2018.10.145**.
26 S. Reichenberger, G. Marzun, M. Muhler and S. Barcikowski, *ChemCatChem*, 2019, **11**, 4489–4518, DOI: **10.1002/cctc.201900666**.
27 (*a*) D. Zhang, J. Liu, P. Li, Z. Tian and C. Liang, *ChemNanoMat*, 2017, **3**, 512–533, DOI: **10.1002/cnma.201700079**; (*b*) R. C. Forsythe, C. P. Cox, M. K. Wilsey and A. M. Müller, *Chem. Rev.*, 2021, **121**, 7568–7637; (*c*) A. A. Manshina, I. I. Tumkin, E. M. Khairullina, M. Mizoshiri, A. Ostendorf, S. A. Kulinich, S. Makarov, A. A. Kuchmizhak and E. L. Gurevich, *Adv. Funct. Mater.*, 2024, **34**, 2405457, DOI: **10.1002/adfm.202405457**; (*d*) D. Zhang, B. Gökce and S. Barcikowski, *Chem. Rev.*, 2017, **117**, 3990–4103.

28 R. Streubel, S. Barcikowski and B. Gökce, *Opt Lett.*, 2016, **41**, 1486–1489.
29 F. Waag, R. Streubel, B. Gökce and S. Barcikowski, *Appl. Nanosci.*, 2021, **11**, 1303–1312, DOI: **10.1007/s13204-021-01693-y**.
30 C. Chen and L. V. Zhigilei, *Appl. Phys. A*, 2023, **129**, 1–35, DOI: **10.1007/s00339-023-06525-0**.
31 M. Spellauge, M. Tack, R. Streubel, M. Miertz, K. S. Exner, S. Reichenberger, S. Barcikowski, H. P. Huber and A. R. Ziefuss, *Small*, 2023, **19**, e2206485.
32 T. Fromme, S. Reichenberger, K. M. Tibbetts and S. Barcikowski, *Beilstein J. Nanotechnol.*, 2024, **15**, 638–663, DOI: **10.3762/bjnano.15.54**.
33 T. Friedenauer, K. Buck, M. Eberwein, A.-L. Bünte, C. Rehbock and S. Barcikowski, *Part. Part. Syst. Char.*, 2023, **40**, 2300034, DOI: **10.1002/ppsc.202300034**.
34 T. Friedenauer, M. Spellauge, A. Sommereyns, C. Rehbock, H. P. Huber and S. Barcikowski, *J. Phys. Chem. C*, 2025, **129**, 6803–6816.
35 P. Wagener and S. Barcikowski, *Appl. Phys. A*, 2010, **101**, 435–439, DOI: **10.1007/s00339-010-5814-x**.
36 T. Fromme, R. Müller, L. Krenz, L. K. Tintrop, I. Sanjuán, T. C. Schmidt, K. M. Tibbetts, C. Andronescu, S. Reichenberger and S. Barcikowski, *J. Phys. Chem. C*, 2025, **129**, 2953–2965.
37 M. Lau and S. Barcikowski, *Appl. Surf. Sci.*, 2015, **348**, 22–29, DOI: **10.1016/j.apsusc.2014.07.053**.
38 A. R. Ziefuß, S. Reichenberger, C. Rehbock, I. Chakraborty, M. Gharib, W. J. Parak and S. Barcikowski, *J. Phys. Chem. C*, 2018, **122**, 22125–22136.
39 F. Waag, Y. Li, A. R. Ziefuß, E. Bertin, M. Kamp, V. Duppel, G. Marzun, L. Kienle, S. Barcikowski and B. Gökce, *RSC Adv.*, 2019, **9**, 18547–18558, DOI: **10.1039/C9RA03254A**.
40 S. Tahir, N. Shkodich, B. Eggert, J. Lill, O. Gatsa, M. Flimelová, E. Adabifiroozjaei, N. M. Bulgakova, L. Molina-Luna, H. Wende, M. Farle, A. V. Bulgakov, C. Doñate-Buendía and B. Gökce, *ChemNanoMat*, 2024, **10**, e202400064, DOI: **10.1002/cnma.202400064**.
41 J. Johny, Y. Li, M. Kamp, O. Prymak, S.-X. Liang, T. Krekeler, M. Ritter, L. Kienle, C. Rehbock, S. Barcikowski and S. Reichenberger, *Nano Res.*, 2022, **15**, 4807–4819, DOI: **10.1007/s12274-021-3804-2**.
42 N. F. Shkodich, I. D. Kovalev, K. V. Kuskov, D. Kovalev, Y. Vergunova, Y. Scheck, S. G. Vadchenko, O. Politano, F. Baras and A. S. Rogachev, *J. Alloys Compd.*, 2022, **893**, 161839, DOI: **10.1016/j.jallcom.2021.161839**.
43 R. Stuckert, F. Pohl, O. Prymak, U. Schürmann, C. Rehbock, L. Kienle and S. Barcikowski, *Beilstein J. Nanotechnol.*, 2025, DOI: **10.3762/bjnano.16.84**.
44 A. S. Rogachev, D. Kovalev, Y. Vergunova, S. G. Vadchenko, D. O. Moskovskikh, N. Yurchenko, E. S. Panina, C. Zhang, O. V. Boyarchenko, Y. Morozov, A. Sheardy, M. Zhukovskyi and A. S. Mukasyan, *J. Alloys Compd.*, 2024, **1002**, 175401, DOI: **10.1016/j.jallcom.2024.175401**.
45 K. S. Kim, M. Couillard, Z. Tang, H. Shin, D. Poitras, C. Cheng, O. Naboka, D. Ruth, M. Plunkett, L. Chen, L. Gaburici, T. Lacelle, M. Nganbe and Y. Zou, *Nat. Commun.*, 2024, **15**, 1450, DOI: **10.1038/s41467-024-45731-z**.
46 D. J. Chakrabarti and D. E. Laughlin, *Bull. Alloy Phase Diagrams*, 1984, **5**, 59–68, DOI: **10.1007/BF02868727**.
47 C.-Y. Shih, M. V. Shugaev, C. Wu and L. V. Zhigilei, *Phys. Chem. Chem. Phys.*, 2020, **22**, 7077–7099, DOI: **10.1039/D0CP00608D**.

48 Q. Chen, L. Shi, G. Xu, M. Hu, M. Peng and Z. Yao, *Colloids Surf., A*, 2025, **709**, 136106, DOI: **10.1016/j.colsurfa.2025.136106**.
49 **https://www.webelements.com/**.
50 G. Paltauf and H. Schmidt-Kloiber, *Appl. Phys. A*, 1999, **68**, 525–531, DOI: **10.1007/s003390050935**.
51 (*a*) A. Pyatenko, H. Wang, N. Koshizaki and T. Tsuji, *Laser Photonics Rev.*, 2013, **7**, 596–604, DOI: **10.1002/lpor.201300013**; (*b*) A. Takami, H. Kurita and S. Koda, *J. Phys. Chem. B*, 1999, **103**, 1226–1232.
52 H. Huang and L. V. Zhigilei, *J. Phys. Chem. C*, 2021, **125**, 13413–13432.
53 T. Fromme, L. K. Tintrop, S. Reichenberger, T. C. Schmidt and S. Barcikowski, *ChemPhysChem*, 2023, **24**, e202300089, DOI: **10.1002/cphc.202300089**.
54 H. Huang and L. V. Zhigilei, *Sci. China: Phys., Mech. Astron.*, 2022, **65**, 1–16, DOI: **10.1007/s11433-021-1881-8**.
55 M. Tack, M. Usama, N. Kazamer, K. S. Exner, M. Brodmann, S. Barcikowski and S. Reichenberger, *ACS Appl. Energy Mater.*, 2024, **7**, 4057–4067.
56 N. G. Simpson and K. M. Tibbetts, *J. Phys. Chem. C*, 2025, **129**, 5383–5392.
57 G. Marzun, H. Bönnemann, C. Lehmann, B. Spliethoff, C. Weidenthaler and S. Barcikowski, *ChemPhysChem*, 2017, **18**, 1175–1184, DOI: **10.1002/cphc.201601315**.
58 (*a*) T. Simao, D. M. Chevrier, J. Jakobi, A. Korinek, G. Goupil, M. Lau, S. Garbarino, P. Zhang, S. Barcikowski, M.-A. Fortin and D. Guay, *J. Phys. Chem. C*, 2016, **120**, 22635–22645; (*b*) D. Zhang, Z. Ma, M. Spasova, A. E. Yelsukova, S. Lu, M. Farle, U. Wiedwald and B. Gökce, *Part. Part. Syst. Charact.*, 2017, **34**, 1600225.
59 (*a*) J. R. Anderson, Doctoral dissertation, Massachusetts Institute of Technology, 1946, **https://dspace.mit.edu/bitstream/handle/1721.1/82742/27002020-mit.pdf**; (*b*) R. B. McLellan, *Scr. Metall.*, 1969, **3**, 389–391, DOI: **10.1016/0036-9748(69)90262-2**.
60 (*a*) C.-C. Hu and Y.-R. Wu, *Mater. Chem. Phys.*, 2003, **82**, 588–596, DOI: **10.1016/S0254-0584(03)00316-X**; (*b*) J. Haenen, W. Visscher and E. Barendrecht, *Electrochim. Acta*, 1986, **31**, 1541–1551, DOI: **10.1016/0013-4686(86)87073-6**.
61 C. Luan, D. Escalera-López, U. Hagemann, A. Kostka, G. Laplanche, D. Wu, S. Cherevko and T. Li, *ACS Catal.*, 2024, **14**, 12704–12716.
62 (*a*) G. Marzun, A. Levish, V. Mackert, T. Kallio, S. Barcikowski and P. Wagener, *J. Colloid Interface Sci.*, 2017, **489**, 57–67, DOI: **10.1016/j.jcis.2016.09.014**; (*b*) K. Lian, S. J. Thorpe and D. W. Kirk, *Electrochim. Acta*, 1992, **37**, 2029–2041, DOI: **10.1016/0013-4686(92)87119-K**; (*c*) D. E. Pissinis, L. E. Sereno and J. M. Marioli, *Open J. Phys. Chem.*, 2012, **02**, 23–33.
63 L. Dai, C. Fang, F. Yao, X. Zhang, X. Xu, S. Han, J. Deng, J. Zhu and J. Sun, *Appl. Surf. Sci.*, 2023, **623**, 156991, DOI: **10.1016/j.apsusc.2023.156991**.
64 K. M. Cole, Amorphous Ni-Based Alloys as Alkaline Oxygen Evolution Electrocatalysts, Doctoral dissertation, University of Toronto, 2022.
65 A. M. Zaky and F. H. Assaf, *Br. Corros. J.*, 2002, **37**, 48–55.
66 J. Kang, F. Li, Z. Xu, X. Chen, M. Sun, Y. Li, X. Yang and L. Guo, *JACS Au*, 2023, **3**, 2660–2676, DOI: **10.1021/jacsau.3c00418**.
67 S.-X. Liang, L.-C. Zhang, S. Reichenberger and S. Barcikowski, *Phys. Chem. Chem. Phys.*, 2021, **23**, 11121–11154, DOI: **10.1039/D1CP00701G**.
68 X. Xu, Y. Guo, B. P. Bloom, J. Wei, H. Li, H. Li, Y. Du, Z. Zeng, L. Li and D. H. Waldeck, *ACS Nano*, 2020, **14**, 17704–17712.

69 D. Guan, W. Zhou and Z. Shao, *Small Sci.*, 2021, **1**, 2100030, DOI: **10.1002/smsc.202100030**.
70 J. Chantaramethakul, C. Hussakan, Y. Yenmankhong, P. Chandeang, R. Techapiesancharoenkij, W. Hirunpinyopas, Kasmui, C. Kurniawan and G. Panomsuwan, *RSC Adv.*, 2024, **14**, 31648–31654, DOI: **10.1039/D4RA04809A**.
71 (*a*) M. Ławrywianiec, J. Smajdor, B. Paczosa-Bator and R. Piech, *Anal. Methods*, 2017, **9**, 6662–6668, DOI: **10.1039/C7AY02140B**; (*b*) J. Smajdor, R. Piech, M. Pięk and B. Paczosa-Bator, *J. Electroanal. Chem.*, 2017, **799**, 278–284, DOI: **10.1016/j.jelechem.2017.06.013**.
72 D. Amans, M. Diouf, J. Lam, G. Ledoux and C. Dujardin, *J. Colloid Interface Sci.*, 2017, **489**, 114–125, DOI: **10.1016/j.jcis.2016.08.017**.
73 S. Harris, E. Kaplan, M. Aftel and K. M. Tibbetts, *J. Phys. Chem. B*, 2024, **128**, 10481–10491.
74 L. Lutterotti, *MAUD tutorial-instrumental broadening determination*, Universita di Trento, 38050 Trento, Italy, 2006, pp. 1–18.
75 L. Wang, D. Mercier, S. Zanna, A. Seyeux, M. Laurent-Brocq, L. Perrière, I. Guillot and P. Marcus, *Corros. Sci.*, 2020, **167**, 108507, DOI: **10.1016/j.corsci.2020.108507**.